

Effects of oscillating spacetime metric background on a complex scalar field and formation of topological vortices

Shreyansh S. Dave^{1,*} and Sanatan Dikal^{1,2,†}

¹*The Institute of Mathematical Sciences, Chennai 600113, India*

²*Homi Bhabha National Institute, Training School Complex, Anushakti Nagar, Mumbai 400085, India*

We study the time evolution of a complex scalar field in the symmetry broken phase in the presence of oscillating spacetime metric background. In our (2+1)-dimensional simulations, we show that the spacetime oscillation can excite an initial field configuration, which ultimately leads to the formation of topological vortices in the system. At late times, field configuration achieves a *disordered state*. A detailed study of the momentum and frequency modes of the field reveals that these field excitations are driven by the phenomena of *parametric resonance*. For a suitable choice of parameters of the simulation, we observe a persistent lattice structure of vortex-antivortex pairs. We discuss applications of this study to the dynamics of interior superfluidity of neutron stars during the binary neutron star mergers, in generation of excitations of ultralight axion-like field and associated coherent emission of particles, etc.

I. INTRODUCTION

Topological defects arise in systems ranging from condensed matter to the early Universe [1, 2]. They exist in systems which have topologically non-trivial order parameter space (or vacuum manifold). There are many condensed matter systems, such as superfluid, superconductor, nematic liquid crystal etc., which have topologically non-trivial order parameter space in their respective symmetry broken phases, therefore allow the existence of topological defects. For example, the superfluid phase of ${}^4\text{He}$ is characterized by a complex wavefunction. The corresponding order parameter space is a circle S^1 , for which the *fundamental group* is non-trivial, i.e. $\pi_1(S^1) = \mathcal{Z}$. Therefore this system allows the existence of topological vortices [3]. The vortices are characterised by different elements of the fundamental group.

There are various ways by which topological defects can form in a physical system. These defects produce during a spontaneous symmetry breaking phase transition, which can be described by the *Kibble mechanism* [4]. There are other methods also by which topological defects can be nucleated in a system. For example, in superfluid ${}^4\text{He}$, the rotation of vessel within a range of angular velocity leads to the generation of vortex lattice [5, 6]. Similarly, in the type-II superconductor, an external magnetic field within a range of field strength leads to the formation of flux-tube lattice [5, 6].

In refs.[7, 8], the formation of defect-antidefect pairs has been studied in Φ^4 theories with time dependent temperature in the effective potential. The temperature is considered to be periodically oscillating with $T(t) < T_c$, where T_c is the transition temperature below which symmetry of the theory spontaneously broken. Due to $T^2\Phi^2$ term, minima of the effective potential periodically oscillates. This oscillation induces field excitations (mainly longitudinal excitations) via the *parametric resonance* of the field. The parametric resonance occurs when the fre-

quency of temperature oscillation matches with the mass of the field. These excitations ultimately leads to the formation of vortex-antivortex pairs in U(1)-theory [7] and kink-antikink pairs in \mathcal{Z}_2 -theory [8].

In Bose-Einstein condensate (BEC) of trapped ultracold atoms, a new mechanism of formation of superfluid vortices has been studied in refs.[9, 10]. In these studies, vortex-antivortex pairs are generated by periodically varying trapping potential of BEC condensate. Note that the dynamics of superfluid is governed by the time-dependent Gross-Pitaevskii equation (GPE), solution of which gives a coherent wavefunction of BEC condensate [11]. These studies suggest that under the perturbation, time dependent excitations arise in the condensate modifying the coherent wavefunction. These excitations lead to the formation of vortex-antivortex pairs in the system. Subsequently, a tangled network of vortices forms in the system signalling transition to a state of quantum turbulence. Ultimately, BEC condensate reaches a disordered state. In the study, the oscillation frequency of trapping potential is taken 200 Hz, and the time scale for the whole process is few tens of millisecond. Note that this time scale depends upon the amplitude and frequency of oscillation of trapping potential (i.e. rate of injected energy) and the energy of the vortex configuration in the system.

Following the above studies in refs.[7–10], it is an obvious question to ask if spacetime oscillation can also induce parametric resonance or large oscillations in the field Φ . Such a question is relevant for many systems, for example ultralight axion-like field coupled to gravitational wave, neutron star under a time dependent tidal deformations, etc. The dynamical and thermal evolution of a neutron star, in terms of periodic glitches and cooling rate respectively, strongly support the existence of neutron superfluidity in the interior regions of star [12, 13]. The theoretical studies suggest the presence of 1S_0 neutron superfluidity in the inner crust region, while 3P_2 neutron superfluidity as well as 1S_0 proton

superconductivity in the outer core region [13]. In the inner core region there is also possibility of existence of *color superconducting phases* of quantum chromodynamics (QCD) [14]. During a binary neutron stars (BNS) merger, the orbiting neutron stars exert a time dependent tidal force on each other [15]. The frequency and amplitude of this tidal force keep on increasing with time, and become maximum towards the end of merger. Under such tidal force, depending upon the *tidal deformability*, neutron star undergoes a time dependent deformations. These tidal deformations can couple to the condensate of interior superfluid of neutron star and may lead to the turbulence (formation of tangled vortices) as discussed in refs.[9, 10]. Here, we mention that a similar kind of scenario, e.g. occurrence of superfluid turbulence, superfluid to normal fluid transition, and glitch (or anti-glitch) in neutron stars during a BNS merger has been discussed in ref.[16].

We mention that the *tidal deformability* of a neutron star depends upon the equation of state of its interior medium [15]. The spin motion of neutron stars may also affect its deformations during the merger. Note that due to the tidal force during the merger, energy pumped into the system is so high that the temperature and density of neutron star can reach up to 100 MeV and few times of nuclear saturation density, respectively [17]. In such situation neutron superfluidity can be destroyed even before the merger as the transition temperature for such superfluidity lies in between 0.1 MeV to few MeV.

In order to study the time evolution of superfluid inside neutron star under such time dependent tidal deformation, one must solve the relativistic Gross-Pitaevskii equation, known as the Gross-Pitaevskii-Anandan equation [18], in the background of spacetime metric of star with a time dependent perturbation appropriate for the BNS merger system. This study can also be done by solving non-linear Klein-Gordon equation in an appropriate metric background, as superfluidity can also be described in the field theoretical framework, where BEC is generally characterized by spontaneous breaking of U(1) global symmetry for a complex scalar field $\Phi = \Phi_0 e^{i\theta}$ [19, 20]. In this description, the condensate density ρ_s is related with the vacuum expectation value (VEV) of the field as $\rho_s = \Phi_0^2/\xi_s$, where ξ_s is the correlation length [20]. A spatial variation of phase θ of the field gives flow to the superfluid. The metric oscillation mentioned above may generate excitations in the field Φ and lead to the formation of vortex-antivortex pairs in the interior superfluid of neutron star.

In this paper, we study the effects of spacetime oscillation on the evolution of a complex scalar field. This may shade some light on the time dynamics of interior superfluidity of neutron star during the merger. However, here instead of considering a spacetime metric of star, for simplicity we take Minkowski metric with a periodic perturbation in time. This simplification helps to

give a clear understanding of the effect of metric oscillation on the field and production of topological vortices. In this metric background, we numerically solve the non-linear Klein-Gordon equation in (2+1)-dimensions for the time evolution of a complex scalar field with an initial field configuration given by, $\Phi(x, y) = \Phi_0 + \delta\Phi(x, y)$, where Φ_0 is the VEV of U(1)-broken effective potential and $\delta\Phi(x, y)$ represents small fluctuations of field about the VEV. Here, the initial field fluctuations are considered, as the spacetime oscillation couples with the field equation only through the spacetime derivatives of the field; see equation of motion below.

We see that under the spacetime oscillation, field undergoes large amplitude oscillation for a wide range of frequencies of metric oscillation, which eventually leads to the formation of vortex-antivortex pairs. In the low frequency regime (frequency smaller than the mass of field) mainly transverse modes (Goldstone modes) arise, while in the high frequency regime, longitudinal modes also get generated. A detailed analysis shows that there is a correspondence between the frequency of spacetime oscillation and momentum of time growing field-modes. This suggests that the field undergoes *parametric resonance* under the spacetime oscillation.

We mention that our present study is fundamentally different from the previous studies in refs.[7, 8], even though the underlying physics for the generation of topological defects is same, i.e. *parametric resonance*. In previous studies oscillating temperature couples to the magnitude of the field. Therefore, in order to observe parametric resonance, the frequency of temperature oscillation must be close to the mass of longitudinal modes of the field. In present case, the spacetime oscillation couples to the gradient of the field. This makes a direct coupling between the frequency of spacetime oscillation to the momentum of field-modes present in the initial field configuration. Therefore by satisfying the resonant condition, some specific field-modes grow exponentially with time. This can occur, as far as the appropriate momentum-modes of the field are present in the system. Thus, in present case there is no lowest frequency cut-off to induce parametric resonance, and vortex-antivortex pairs form for a wide range of frequencies of spacetime oscillation. The time of formation of first vortex-antivortex pair in the system is inversely related with the frequency of spacetime oscillation, and diverges as frequency approaches zero.

This paper is organized as follows. In section-II, we derive the equation of motion for a complex scalar field in the presence of oscillating spacetime metric background. In section-III, we outline the details of our numerical simulations. Then we present our simulation results in section-IV. Finally, we briefly summarize our work and give future outlook in section-V.

II. EQUATION OF MOTION

In order to study the effects of spacetime oscillation on a complex scalar field, we consider the spacetime metric as a periodic perturbation on the top of the Minkowski metric. We consider the *inverse* spacetime metric as, $g^{\mu\nu} \equiv \text{diag}(-1, 1 - \varepsilon \sin(\omega(t-z)), 1 + \varepsilon \sin(\omega(t-z)), 1)$, where ε (< 1) and ω are the amplitude and frequency of spacetime oscillation, respectively; $(-t, x, y, z)$ are spacetime coordinates. Note that this form of the metric is chosen just for a simplicity in the equation of motion of the field, though any periodic time-dependent metric can be taken for our study. The action of the complex scalar field on the spacetime manifold with the above metric is [20, 21],

$$S = \int d^4x \sqrt{-g} \left[-\frac{1}{2} g^{\mu\nu} \partial_\mu \Phi^* \partial_\nu \Phi - V(\Phi^* \Phi) \right], \quad (1)$$

where, $g = \det(g_{\mu\nu}) = -(1 - \varepsilon^2 \sin^2(\omega(t-z)))^{-1}$, $\Phi = \phi_1 + i\phi_2$, $\Phi^* = \phi_1 - i\phi_2$; ϕ_1 and ϕ_2 are the real scalar fields. We consider the following symmetry breaking effective potential,

$$V(\Phi^* \Phi) = \frac{\lambda}{4} (\Phi^* \Phi - \Phi_0^2)^2, \quad (2)$$

where, λ is the self-interaction coupling parameter of the field, and Φ_0 is the VEV of the effective potential. With this, $m_\Phi = \Phi_0 \sqrt{\lambda}$ is the mass of the longitudinal mode of the field. The equation of motion for (ϕ_1, ϕ_2) fields are [20, 21],

$$\square \phi_i - \frac{dV}{d\phi_i} = 0, \quad (3)$$

where, $i = 1, 2$. The covariant d'Alembertian is given by,

$$\square \phi_i = \frac{1}{\sqrt{-g}} \partial_\mu (\sqrt{-g} g^{\mu\nu} \partial_\nu \phi_i). \quad (4)$$

Therefore in the expanded form, the field equations are,

$$\begin{aligned} & -\frac{1}{2} \frac{\varepsilon^2 \omega \sin(2\omega(t-z))}{(1 - \varepsilon^2 \sin^2(\omega(t-z)))} \left(\frac{\partial \phi_i}{\partial t} + \frac{\partial \phi_i}{\partial z} \right) - \frac{\partial^2 \phi_i}{\partial t^2} \\ & + (1 - \varepsilon \sin(\omega(t-z))) \frac{\partial^2 \phi_i}{\partial x^2} + (1 + \varepsilon \sin(\omega(t-z))) \frac{\partial^2 \phi_i}{\partial y^2} \\ & + \frac{\partial^2 \phi_i}{\partial z^2} - \lambda \phi_i (\phi_1^2 + \phi_2^2 - \Phi_0^2) = 0. \end{aligned} \quad (5)$$

For the simplicity of solving it numerically, (i) we assume that there is no variation of the field Φ along z -direction, and (ii) we look at the solution of the field only in the

$z=0$ plane. With these simplifications, the above equations reduce to,

$$\begin{aligned} & -\frac{1}{2} \frac{\varepsilon^2 \omega \sin(2\omega t)}{(1 - \varepsilon^2 \sin^2(\omega t))} \frac{\partial \phi_i}{\partial t} - \frac{\partial^2 \phi_i}{\partial t^2} + (1 - \varepsilon \sin(\omega t)) \frac{\partial^2 \phi_i}{\partial x^2} \\ & + (1 + \varepsilon \sin(\omega t)) \frac{\partial^2 \phi_i}{\partial y^2} - \lambda \phi_i (\phi_1^2 + \phi_2^2 - \Phi_0^2) = 0. \end{aligned} \quad (6)$$

It is very clear from the above equations, that the spacetime oscillation only couples to the derivatives of the field. Note that in the equations, the coefficient of first order time derivative has an oscillation with a mixture of frequencies ω and 2ω . Under the spacetime oscillation, gradient of the field oscillates, which must induce oscillation in the field via the *parametric resonance* with the oscillation frequency ω and possibly with 2ω . This field oscillation must be modulated by the steep rise of the effective potential in the longitudinal direction. The parametric resonance of the field eventually leads to the formation of vortex-antivortex pairs in the system. Our simulation results validate these expectations, which we present in the following sections.

III. SIMULATION DETAILS

To perform the simulation, we discretize the xy -plane into 200×200 lattice points with the lattice spacing of $\Delta x = \Delta y = 0.01 \Lambda$, giving the total lattice size of 2.0Λ in each direction (here, Λ is a unit of length and time, which we haven't specified, as in this work we are not giving phenomenological prediction for any system). Δx and Δy should be smaller than inverse of the field-mass, i.e. $\Delta x, \Delta y < m_\Phi^{-1}$, so that a reasonable spatial variation of the field can be resolved. The time is discretized in the time step of $\Delta t = 0.005 \Lambda$. Note that in the equation of motion (Eq.(6)), the discretization in the time-axis works only if the condition $\Delta t < \omega^{-1}$ satisfies. In our simulation, we study the effects of spacetime oscillation, in particular, the role of parameters ε and ω on the field evolution. To describe the effects, for most of the simulations, we consider $\varepsilon = 0.4$ and $\omega = 100 \Lambda^{-1}$. We take the parameters of the effective potential as $\Phi_0 = 10 \Lambda^{-1}$ and $\lambda = 40$. We also point out how the results vary with these parameters.

In Eq.(6), the field evolution is coupled with spacetime oscillation through second order spatial derivative and first order time derivative of the field. Therefore initial field configuration can respond to the spacetime oscillation only when fluctuations of the field (spacetime gradient) be present in the system (i.e. iff the field configuration is not in its complete minimum energy configuration), which can naturally arise due to the presence of thermal and/or quantum fluctuations. For simplicity, we consider fluctuations only in the initial field configu-

ration, i.e. we take $\Phi(x, y) = \Phi_0 + \delta\Phi(x, y)$ at time $t = 0$ and evolve with Eq.(6).

In our simulation, for the initial field configuration, we have considered small spatial variations in ϕ_1 and ϕ_2 fields such that the magnitude remains Φ_0 , i.e the field is taken at the minima of the effective potential (Eq.2) and only transverse fluctuations of the field has been considered for the simulation. However, we have seen that considering fluctuations in the magnitude of the field doesn't change any qualitative aspect of the simulation results. More specifically, we have taken $\phi_1(x, y, t=0) = \Phi_0 \sqrt{1 - \alpha_{xy}^2}$ and $\phi_2(x, y, t=0) = \Phi_0 \alpha_{xy}$, where α_{xy} varies randomly from point to point on the lattice in the range $[-\beta, \beta]$; here $0 < \beta \ll 1$. This initial field configuration has a non-zero spatial gradient of both the fields. In our simulation, we have taken $\beta = 0.2$. However, we have seen that choosing different β doesn't change results qualitatively. We evolve this initial field configuration by solving Eq.(6) using second order Leapfrog method, and considering periodic boundary condition along the spatial directions.

IV. SIMULATION RESULTS

A. Parametric resonance of field under spacetime oscillation

We now present our simulation results. In Fig.1, we have shown the vector plots of field configuration in the physical space (xy -plane) at four different times. The x - and y -components of the vector field correspond to ϕ_1 and ϕ_2 fields, respectively. Note that the whole lattice area is $2.0 \times 2.0 \Lambda^2$, but we have shown only a small portion of the lattice. In this simulation, we have taken $\varepsilon = 0.4$, $\omega = 100 \Lambda^{-1}$, $\Phi_0 = 10 \Lambda^{-1}$, and $\lambda = 40$. As we have mentioned earlier, we take random transverse fluctuations in the initial field configuration, therefore phase of the field varies randomly from one lattice point to other within the range of $\pm 0.2 \text{ rad}$ for the given value of β . Fig.1(a) corresponds to the initial field configuration (at time $t=0$), where one can see such phase fluctuations on the lattice points. We observe that roughly during the time interval of $0.5 - 1.5 \Lambda$, the field itself starts performing spacetime oscillations with a significantly large amplitude; at time larger than this, field dynamics becomes much more complicated. Fig.1(b) shows the field configuration at $t=1.3 \Lambda$. This figure clearly shows that there is generation of a systematic periodic variation (wave) of the field in the physical space. The amplitude of this wave increases with time. We observe that the wavelength of this wave is ω dependent; by decreasing ω , the wavelength of this wave increases (see Fig.4 and Fig.5 in this regard). Due to such spatial variations, the field acquires a significant gradient energy in some parts of

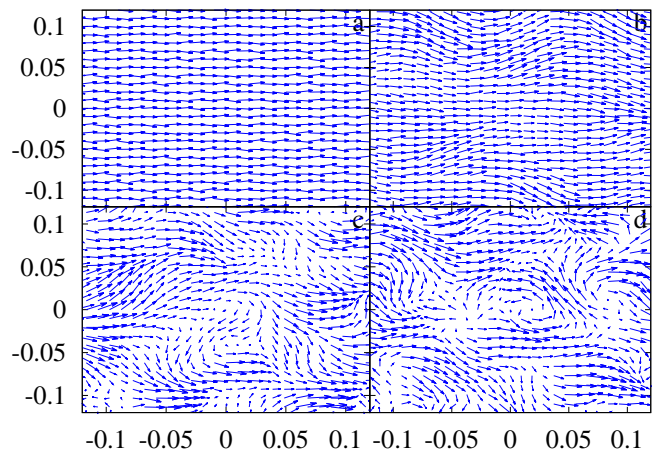


FIG. 1: Figure shows the vector plots of field configuration in physical space (xy -plane) at four time steps of field evolution. The parameters of simulation are $\varepsilon=0.4$, $\omega=100 \Lambda^{-1}$, $\Phi_0=10 \Lambda^{-1}$, $\lambda=40$. Plots (a),(b),(c), and (d) correspond to the field configurations at time $t=0$, 1.35 , 1.7 , and 1.8Λ , respectively. In plot(d) vortex-antivortex pairs has been formed. Roughly at time $t=2.5 \Lambda$ field configuration achieves a *disordered state*.

the physical space to climb the central barrier of the effective potential and fall into the opposite side of the vacuum manifold. This leads to the formation of vortex-antivortex pairs in the system. This process can be seen in Fig.1(c) and Fig.1(d) which are plotted at time $t=1.7 \Lambda$ and $t=1.8 \Lambda$, respectively. The vortex-antivortex pairs appear and disappear in the system, and the overall number of pairs keeps on increasing with time. Roughly at the time $t=2.5 \Lambda$, fluctuations become so strong, that the field configuration no longer remains in the *ordered state* and achieves a *disordered state* (not shown in the figure).

In Fig.2, we have plotted distribution of the field in the $\phi_1\phi_2$ -plane (field-space) at four different times. (In this figure, the field has been mapped from the physical space to the field-space.) The density of points is indicated by colors in the figure. The parameters of simulation are same as that in Fig.1. Fig.2(a) shows the field distribution at time $t=0.05 \Lambda$, which is highly localized around $\phi_1 \approx \Phi_0 = 10 \Lambda^{-1}$ and $\phi_2 \approx 0$ due to our choice of initial field configuration. In Fig.2(a), the maximum height of the distribution is 2672. Note that we have normalized the distribution such that in each case the density varies between 0 and 1. As field evolves, the distribution keeps on spreading around the initial distribution in the field-space. Fig.2(b) shows the field distribution at time $t=1.05 \Lambda$ with maximum distribution height of 316. One can clearly see that at this time, mostly the transverse excitations have been generated. Fig.2(c) shows the stage of field distribution at time $t=1.35 \Lambda$ with distribution height of 88. By this time, both kind of excitations, transverse as well as longitudinal, have been generated

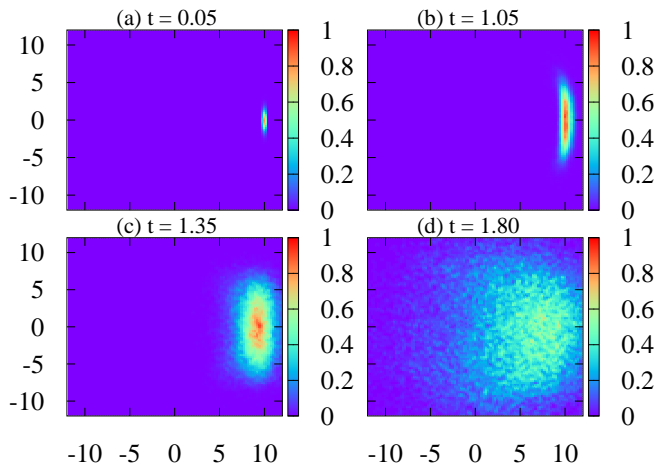


FIG. 2: In the figure, we have plotted distribution of field in the field-space ($\phi_1\phi_2$ -plane) at four different times of field evolution. Note that we have normalized the distribution such that each density plot gets variation in between 0 and 1. Plots (a),(b),(c), and (d) correspond to time steps $t=0.05$, 1.05 , 1.35 , and 1.8Λ , respectively. In plot(a), field distribution is highly localized about the chosen minima of the effective potential, which becomes more spread in plot(b), where mostly transverse excitations have been generated. In plot(c) longitudinal excitations also have been generated. At the time stage of plot(d), field flips to the opposite side of the effective potential leading to the formation of vortex-antivortex pairs.

in the system. Note that Fig.2(b) and Fig.2(c) correspond to the time duration in which field oscillates with a significantly large amplitude, as shown in Fig.1(b). It is very clear from Fig.2(b) and Fig.2(c), that initially transverse excitations arise in the system, which causes a significantly large gradient energy leading to the generation of longitudinal excitations as well. These excitations ultimately leads to the formation of vortex-antivortex pairs in the system. The field distribution, at the time stage when these pairs have been formed, is shown in Fig.2(d) at $t=1.8 \Lambda$ with maximum distribution height of 26. Subsequently, the field distribution spreads over the field-space symmetrically about $\phi_1=\phi_2=0$. The maximum extent of this distribution becomes way beyond Φ_0 signalling U(1) symmetry restoration.

To see how fluctuations in fields ϕ_1 and ϕ_2 grow with time, we calculate field's fluctuations $\delta\phi_i(t)=\sqrt{\langle\phi_i^2(\vec{x},t)\rangle - \langle\phi_i(\vec{x},t)\rangle^2}$, where $i=1,2$, and bracket $\langle\dots\rangle$ represents the volume average of the field. Fig.3 shows the time evolution of $\delta\phi_1$ and $\delta\phi_2$ for two sets of parameters of the effective potential. The parameters of spacetime metric for the simulations are $\varepsilon=0.4$ and $\omega=100 \Lambda^{-1}$, same as used in Figs.1,2. Plots (a)(blue) and (b)(gray) are the time evolution of $\delta\phi_1$ and $\delta\phi_2$ for $\Phi_0=10 \Lambda^{-1}$ and $\lambda=40$, while plots (c)(black) and (d)(red) are the time evolution of $\delta\phi_1$ and $\delta\phi_2$ for $\Phi_0=0.1 \Lambda^{-1}$ and $\lambda=4$, respectively. Note that ϕ_2 at initial time is proportional to Φ_0 , that is

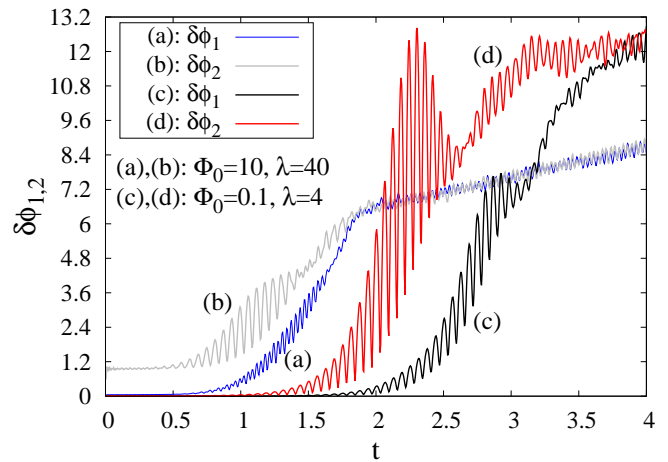


FIG. 3: Figure shows the time evolution of growth of fluctuations $\delta\phi_1$ and $\delta\phi_2$ of fields ϕ_1 and ϕ_2 , respectively, under the spacetime oscillation for two sets of parameters of the effective potential. The parameters of spacetime metric are $\varepsilon=0.4$ and $\omega=100 \Lambda^{-1}$. Plots (a)(blue) and (b)(gray) are the time evolution of $\delta\phi_1$ and $\delta\phi_2$ for $\Phi_0=10 \Lambda^{-1}$ and $\lambda=40$, while plots (c)(black) and (d)(red) are for $\Phi_0=0.1 \Lambda^{-1}$ and $\lambda=4$, respectively. Figure clearly shows that in each case, the initial growth of $\delta\phi_2$ is larger in comparison with $\delta\phi_1$; both ultimately become degenerate. Note that there is oscillation in plot(a) and plot(b) during the time interval of $0.5 - 1.5 \Lambda$, which is related with the field oscillation discussed in Fig.1.

the reason $\delta\phi_2$ starts with larger value in plot (b) in comparison with plot (d), even though the chosen value of β in both the cases are same (indeed, the fluctuations in phase of field are same for both sets of parameter of the effective potential). Figure clearly shows that in each case, the growth of fluctuation in ϕ_2 field is larger than in ϕ_1 . This depends upon our choice of initial field configuration. After some time, both the field fluctuations become degenerate. Note that there is oscillation in plots (a) and (b) during the time interval of $0.5 - 1.5 \Lambda$, which corresponds to the stage of large amplitude *field oscillation* as discussed in Fig.1.

Even though the shape of effective potential modulates the dynamics of field, plots show that there is not much qualitative difference in the growth of fluctuations by changing the parameters of the effective potential (see Fig.6 also). Here it should be noted that for $\Phi_0=10 \Lambda^{-1}$, $\lambda=40$, and for $\Phi_0=0.1 \Lambda^{-1}$, $\lambda=4$, mass of the field m_Φ are $63.24 \Lambda^{-1}$ and $0.2 \Lambda^{-1}$, respectively. So for former case, m_Φ is roughly in the same order of ω , while for later case, it is three orders of magnitude smaller. Thus, even in such a huge range of m_Φ , for which $\omega > m_\Phi$, the evolution of these fluctuations are qualitatively same. Next, we show that there is a fundamental difference in the evolution of field for $\omega \gtrsim m_\Phi$ and for $\omega < m_\Phi$.

In order to further investigate the behavior of field configurations at various time stages, we calculate the time evolution of various momentum-modes of the fields ϕ_1

and ϕ_2 . The Fourier transform of the field configuration from the physical space to the momentum space at any time is given by,

$$\tilde{\phi}_i(\vec{k}, t) = \frac{1}{\mathcal{A}} \int_{b.c.} d^2\vec{x} \phi_i(\vec{x}, t) e^{i\vec{k}\cdot\vec{x}}; \quad i = 1, 2, \quad (7)$$

where \mathcal{A} is the total area of the system, *b.c.* stands for the *boundary condition*, and $\vec{k}=k_x\hat{x}+k_y\hat{y}$, $\vec{x}=x\hat{x}+y\hat{y}$ are the momentum and position vectors, respectively. In Fig.4 and Fig.5, we have plotted modulus of momentum-modes of fields ϕ_1 and ϕ_2 , i.e. $|\tilde{\phi}_1(\vec{k}, t)|$ (upper panel) and $|\tilde{\phi}_2(\vec{k}, t)|$ (lower panel), in the momentum space with spacing $\Delta k_x=\Delta k_y=2.0 \Lambda^{-1}$. In Fig.4, we have taken spacetime oscillation frequency larger than m_Φ , while in Fig.5, frequency is taken smaller than that. Therefore the field dynamics is expected to be different in both the cases. (The white regions in plots correspond to the magnitude larger than the maximum range of legends.) Note that for ϕ_1 field, zero-mode (zero-momentum mode) is the most dominant mode, while for ϕ_2 , zero-mode is very close to zero. This is just because of initially chosen values of these fields. In Fig.4, we have taken $\omega=100 \Lambda^{-1}$, $\varepsilon=0.4$, $\Phi_0=10 \Lambda^{-1}$, $\lambda=40$ for the simulation. From left to right, field-modes are plotted at time $t=0.05, 1.05, 1.35, 1.8 \Lambda$; see Fig.1 and Fig.2 also. Note that the time interval of 0.5 - 1.5 Λ is the time-stage of large amplitude oscillation of the field for the given ω . At the initial time itself, all higher momentum-modes of the field upto $k_x=k_y=2\pi/\Delta x$ are present due to the prescribed random fluctuations, which can be seen in the plot at time $t=0.05 \Lambda$. Under the spacetime oscillation, depending upon the frequency ω , some specific momentum-modes of field grow with time. In the figure, there are noticeable growth of $|\tilde{\phi}_1(\vec{k}, t)|$ at $k_x=15 \Lambda^{-1}$, $k_y=\omega$ and $k_x\approx k_y\approx\sqrt{(\omega^2 - m_\Phi^2)}/2=54.77 \Lambda^{-1}$, and $|\tilde{\phi}_2(\vec{k}, t)|$ at $k_x=0$, $k_y=\omega/2$ and $k_x=\omega/2$, $k_y=0$. The subsequent evolution also leads to the growth of various other momentum-modes of both the fields.

This shows that at frequency $\omega \gtrsim m_\Phi$, along with transverse modes of field, longitudinal modes also get growth, which follows the dispersion relation $|\vec{k}|^2+m_\Phi^2=E^2$, where $E=\omega$. This is not the case when $\omega < m_\Phi$, where mainly transverse modes are expected to get growth, which follow the massless dispersion relation $|\vec{k}|^2=E^2$. In Fig.5, we have taken $\omega=50 \Lambda^{-1}$, $\varepsilon=0.4$, $\Phi_0=10 \Lambda^{-1}$, $\lambda=40$ for the simulation. From left to right, field-modes are plotted at time $t=2.0, 2.5, 3.0, 3.5 \Lambda$. In this case also, the initial distributions of field-modes are same as plotted in Fig.4 at time $t=0.05 \Lambda$ (therefore, not shown again in Fig.5). Note that for the given ω , the time interval of 2.0 - 3.7 Λ corresponds to the large amplitude oscillation of the field. Figure clearly shows that there are noticeable growth of $|\tilde{\phi}_1(\vec{k}, t)|$ at $k_x=0$, $k_y=\omega$, and $|\tilde{\phi}_2(\vec{k}, t)|$ at $k_x=0$, $k_y=\omega/2$. In the intermediate stage of field evolution, there are also growth of $|\tilde{\phi}_1(\vec{k}, t)|$ at

$k_x\approx\omega/2$, $k_y\approx\omega/2$ and $k_x\approx\omega/2$, $k_y\approx 3\omega/2$. In this case also, the subsequent evolution leads to the growth of various other momentum-modes of both the fields. Thus, Fig.4 and Fig.5 show that the field dynamics is fundamentally different at $\omega \gtrsim m_\Phi$ and $\omega < m_\Phi$.

To understand why some specific momentum-modes of the field grow for a given ω , we write the field as $\Phi=\Phi_0+v_1+iv_2$ ($\phi_1=\Phi_0+v_1$, $\phi_2=v_2$), where v_1 and v_2 are small fluctuations of the field about the VEV. We write the equation of motion for these fluctuations keeping term upto linear order in these fields, and then Fourier transform in the momentum space as,

$$\frac{\varepsilon^2\omega \sin(2\omega t)}{2 f(t) f(-t)} \dot{\tilde{v}}_{ik} + \ddot{\tilde{v}}_{ik} + (k_x^2 f(t) + k_y^2 f(-t) + 2m_i^2) \tilde{v}_{ik} = 0, \quad (8)$$

where $\tilde{v}_{ik}\equiv\tilde{v}_i(\vec{k}, t)$, $f(t)=(1-\varepsilon \sin(\omega t))$, $m_1=m_\Phi$, and $m_2=0$. These equations clearly show that \tilde{v}_{1k} and \tilde{v}_{2k} undergo parametric resonance (get resonant growth) if suitable conditions (relations between k_x , k_y , m_i , and ω) are satisfied. We numerically solve these equations and find that there are various resonance conditions for both the fields. For \tilde{v}_{1k} , however, there is a lowest frequency ω cut-off, set by mass m_Φ , below which there is no resonant growth, i.e. for \tilde{v}_{1k} , resonance occurs iff $\omega \gtrsim m_\Phi$. On the other hand, for \tilde{v}_{2k} there is no such frequency cut-off (due to its zero mass), therefore it can undergo parametric resonance even for a lowest frequency ω . For a comparison, if one ignores the first term of the equation for \tilde{v}_{2k} , then in (1+1)-dimensions it takes the form of the *harmonic oscillator equation* with the (time dependent) frequency square $k_{x(y)}^2(1\mp\sin(\omega t))$ [22]. In that case, the oscillator undergoes *parametric resonance* when the condition $k_{x(y)}\simeq n\omega/2$ satisfies, where $n=1,2,3,\dots$ [22]. A similar feature of the resonance can be seen in Fig.4 and Fig.5, where $\tilde{\phi}_2$ grows resonantly at $k_{x(y)}\simeq\omega/2$, $k_{y(x)}\simeq 0$. In these figures there is a qualitative difference in the evolution of $\tilde{\phi}_1$ for $\omega \gtrsim m_\Phi$ and $\omega < m_\Phi$, as for $\omega \gtrsim m_\Phi$ some momentum-modes of the longitudinal component (\tilde{v}_{1k}) grow resonantly. This makes clear that in the frequency regime $\omega \gtrsim m_\Phi$, both components of the field, longitudinal as well as transverse, participate in the resonance process, while in the frequency regime $\omega < m_\Phi$ mainly transverse component. This is important to appreciate that the appropriate momentum-modes of the field corresponding to ω has to be present initially, otherwise resonance will not occur. Thus, under the spacetime oscillation, there is no frequency cut-off for resonance to occur as far as the appropriate momentum-modes of the field are present. Here we point out that the above discussion is based on the linear approximation. In reality, ϕ_1 and ϕ_2 are the coupled fields whose dynamics is modulated by the effective potential. This couples various momentum-modes of the field non-linearly, and makes resonance conditions much more complicated.

The above analysis shows that the higher momentum-

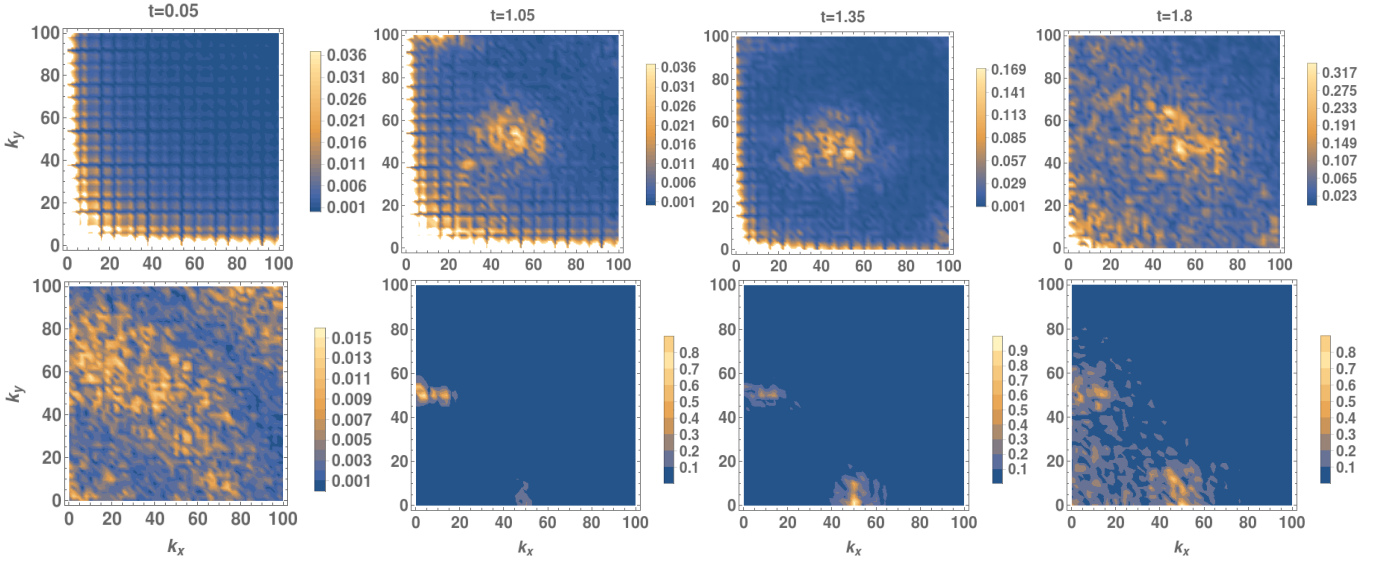


FIG. 4: Figure shows the profile of modulus of field-modes $|\tilde{\phi}_1(\vec{k}, t)|$ (upper panel) and $|\tilde{\phi}_2(\vec{k}, t)|$ (lower panel) at different times for $\omega=100 \text{ \AA}^{-1}$, $\varepsilon=0.4$, $\Phi_0=10 \text{ \AA}^{-1}$, $\lambda=40$. From left to right, modes are plotted at time $t=0.05, 1.05, 1.35, 1.8 \text{ \AA}$. There are noticeable growth of $|\tilde{\phi}_1(\vec{k}, t)|$ at $k_x=15 \text{ \AA}^{-1}$, $k_y=\omega$ and $k_x \approx k_y \approx \sqrt{(\omega^2 - m_\Phi^2)/2} = 54.77 \text{ \AA}^{-1}$, and $|\tilde{\phi}_2(\vec{k}, t)|$ at $k_x=0$, $k_y=\omega/2$ and $k_x=\omega/2$, $k_y=0$. The subsequent evolution also leads to the growth of various other momentum-modes of both the fields.

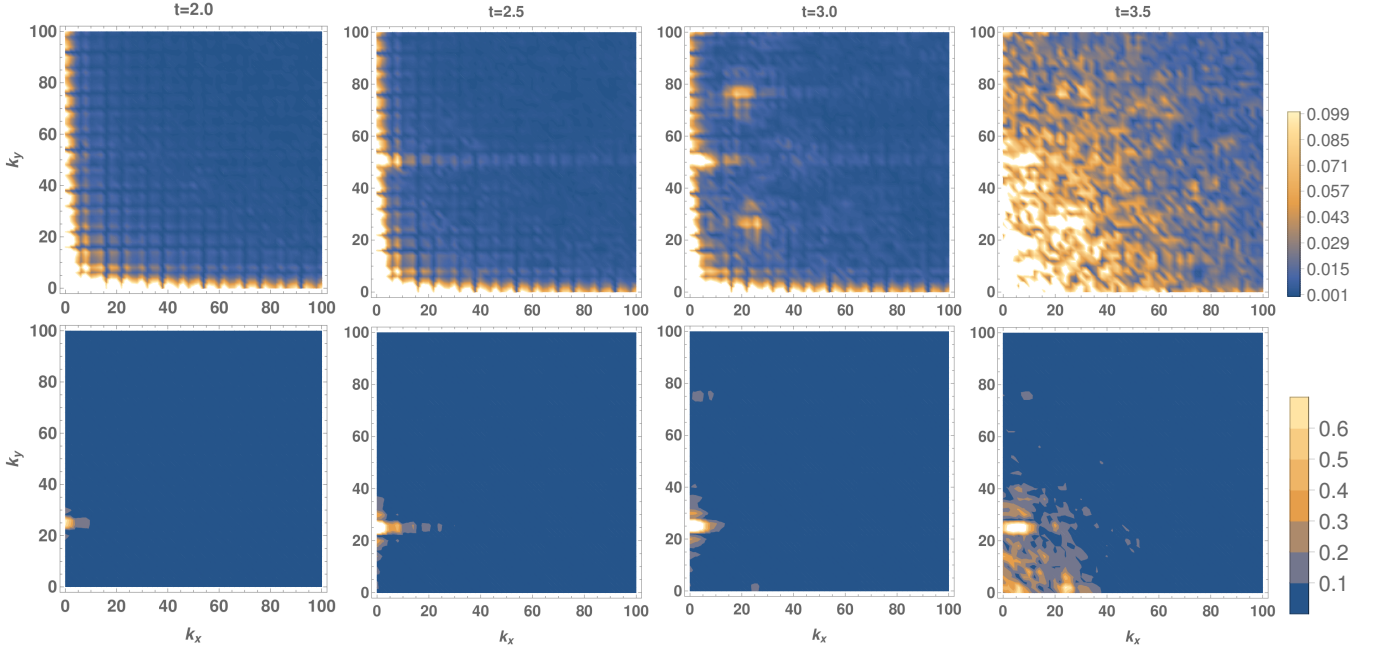


FIG. 5: Figure shows the profile of modulus of field-modes $|\tilde{\phi}_1(\vec{k}, t)|$ (upper panel) and $|\tilde{\phi}_2(\vec{k}, t)|$ (lower panel) at different times for $\omega=50 \text{ \AA}^{-1}$, $\varepsilon=0.4$, $\Phi_0=10 \text{ \AA}^{-1}$, $\lambda=40$. From left to right, modes are plotted at time $t=2.0, 2.5, 3.0, 3.5 \text{ \AA}$. There are noticeable growth of $|\tilde{\phi}_1(\vec{k}, t)|$ at $k_x=0$, $k_y=\omega$, and $|\tilde{\phi}_2(\vec{k}, t)|$ at $k_x=0$, $k_y=\omega/2$. In the intermediate stage of field evolution, there are also growth of $|\tilde{\phi}_1(\vec{k}, t)|$ at $k_x \approx \omega/2$, $k_y \approx \omega/2$ and $k_x \approx \omega/2$, $k_y \approx 3\omega/2$. The subsequent evolution also leads to the growth of various other momentum-modes of both the fields.

modes of fields ϕ_1 and ϕ_2 , following their respective resonance conditions, grow with time. Now, we show how zero-mode of these fields vary with time. The zero-modes of fields characterise the field configuration at each time and provide the frequency of oscillation during the large

amplitude oscillation stage of the field. Fig.6 shows the time evolution of real part of zero-modes ($k_x=0$, $k_y=0$) of fields ϕ_1 and ϕ_2 for two sets of parameters of the effective potential. Note that imaginary part of zero-modes for both the fields are zero. In the figure, zero-mode of

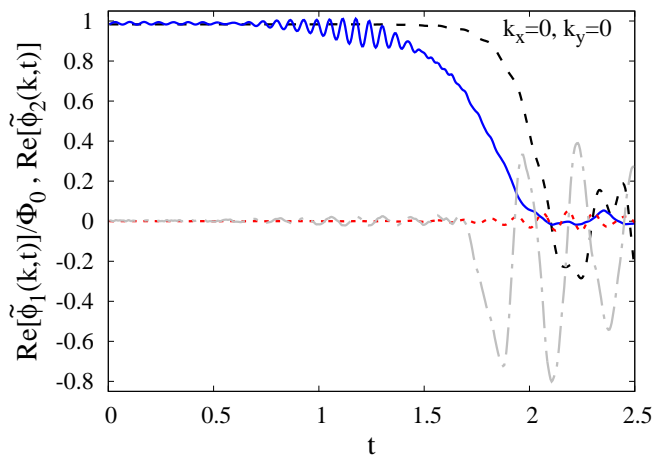


FIG. 6: Figure shows the time evolution of real part of zero-modes of fields ϕ_1 and ϕ_2 for two sets of parameters of effective potential. In the figure, zero-mode of ϕ_1 field is normalized with the respective Φ_0 value. We have taken $\varepsilon=0.4$ and $\omega=100 \Lambda^{-1}$ for the simulation. Solid(blue) and dash-dotted(gray) plots are the time evolution of zero-modes of fields ϕ_1 and ϕ_2 for $\Phi_0=10 \Lambda^{-1}$ and $\lambda=40$, while dashed(black) and dotted(red) plots are for $\Phi_0=0.1 \Lambda^{-1}$ and $\lambda=4$, respectively. Note that there is a small amplitude oscillation in dashed(black) plot, which doesn't appear because of large y -range.

ϕ_1 field is normalized with the respective Φ_0 value. For this simulation, we have taken $\varepsilon=0.4$ and $\omega=100 \Lambda^{-1}$. Solid(blue) and dash-dotted(gray) plots are the time evolution of zero-modes of fields ϕ_1 and ϕ_2 , respectively, for $\Phi_0=10 \Lambda^{-1}$, $\lambda=40$. In this case, there is an oscillation in the ϕ_1 zero-mode during the time interval of $0.5 - 1.5 \Lambda$ with growing and then decaying amplitude (we call it *large amplitude oscillation* stage). From time $t=1.5 \Lambda$ onwards, the oscillation stops and zero-mode starts collapsing towards the zero value. The collapse of zero-mode starts roughly at the time of formation of vortex-antivortex pairs in the system. We have performed the simulations for different spacetime oscillation frequencies and calculated the time evolution of ϕ_1 zero-mode (in the figure, it not shown for other frequencies). We see that in all cases, initially there is a unique frequency and amplitude of oscillation of ϕ_1 zero-mode. Subsequently, this gets modulated with a *new* frequency of oscillation with growing amplitude as shown in Fig.6 from time $t=0.5 \Lambda$. This shows that the very initial time oscillation of ϕ_1 zero-mode (before $t=0.5 \Lambda$ in Fig.6) is independent from the spacetime oscillation, rather, may be related with the evolution of initial field fluctuations. However, the *new* modulation frequency, i.e. the frequency during the time-stage of large amplitude oscillation of ϕ_1 zero-mode, exactly equal to the spacetime oscillation frequency ω (we have shown this later). This gives an another evidence of the *parametric resonance* of the field under the spacetime oscillation.

In Fig.6, ϕ_2 zero-mode, shown by dash-dotted(gray)

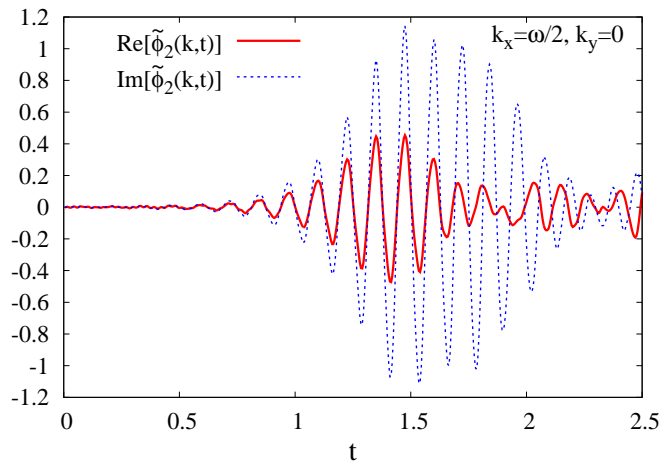


FIG. 7: Figure shows the time evolution of real and imaginary part of $(k_x=\omega/2, k_y=0)$ -mode of field ϕ_2 with solid(red) and dotted(blue) lines, respectively, for $\omega=100 \Lambda^{-1}$, $\varepsilon=0.4$, $\Phi_0=10 \Lambda^{-1}$, $\lambda=40$.

plot, also has small amplitude oscillation roughly in the same time interval of $0.5 - 1.5 \Lambda$, but without much growth. Later, we have shown that the oscillation frequency of zero-mode of ϕ_2 during this time interval is half of the spacetime oscillation frequency. Here, it should be noted that during this time interval, ϕ_2 varies between negative and positive values, spatially as well as temporarily, as can be seen from Fig.1(b). Therefore even though the absolute value of ϕ_2 reaches a non-zero value in some region, its zero-mode comes out to be very small (just because of the cancellation of positive and negative values). It is already clear from Fig.3, that during this time interval, the growth in the fluctuations of field ϕ_2 is larger in comparison with fluctuations in ϕ_1 . Indeed, the higher momentum-modes of ϕ_2 get growth with time, which we have already seen in Fig.4 at $k_x=\omega/2, k_y=0$ and $k_x=0, k_y=\omega/2$. To show this growth in more detail, in Fig.7, we have plotted the time evolution of real and imaginary part of $(k_x=\omega/2, k_y=0)$ -mode of ϕ_2 with solid(red) and dotted(blue) lines, respectively. This clearly shows an oscillation of these modes with growing and then decaying amplitude.

To show the dependence of the zero-modes of fields ϕ_1 and ϕ_2 on the parameters of effective potential, in Fig.6 we have also plotted their time evolution for $\Phi_0=0.1 \Lambda^{-1}$ and $\lambda=4$ with dashed(black) and dotted(red) lines, respectively. In this case, depth of the effective potential is very small, therefore the field can easily overcome the central barrier at $\Phi=0$. Note that in this case, the amplitude of ϕ_1 zero-mode oscillation is small, which is not clearly visible because of the large y -range in the plot. The oscillation in ϕ_2 zero-mode doesn't have a significant amplitude because of the reason mentioned above.

In order to determine the oscillation frequency of fields during the time interval, say t_i and t_f , in which ϕ_1 zero-

mode oscillates with a significantly large amplitude, we perform Fourier transform of fields' zero-mode from t -space to the frequency f -space,

$$\Pi_i(\vec{k}, f) = \frac{1}{(t_f - t_i)} \int_{t_i}^{t_f} dt \tilde{\phi}_i(\vec{k}, t) e^{-ift}; \quad i = 1, 2. \quad (9)$$

We calculate the *modulus* of $\Pi_1(\vec{k}, f)$ and $\Pi_2(\vec{k}, f)$ fields, which provide the frequency spectrum of momentum-modes of ϕ_1 and ϕ_2 . Fig.8 shows the frequency spectrum of zero-mode of field ϕ_1 during the mentioned time interval for different spacetime oscillation frequencies ω . In the figure, the time interval $t_i - t_f$ for each frequency ω has been mentioned in brackets. To obtain this frequency spectrum, in each case we have subtracted Φ_0 from the zero-mode of ϕ_1 so that the background frequency modes, arise due to constant Φ_0 value, get eliminated and the peak structure become apparent. (However, this subtraction doesn't remove background frequency modes completely, that is the reason a peak at the zero frequency is still present in each plot). In the figure, violet(dotted), green(solid thin), and black(solid thick) lines corresponds to the frequency spectrum for 20, 50, and 100 Λ^{-1} frequencies of spacetime oscillation, respectively. Note that in each case, $\varepsilon=0.4$, $\Phi_0=10 \Lambda^{-1}$, and $\lambda=40$, as taken earlier. It is very clear from the figure, that in each case frequency spectrum has a peak at their respective frequency ω of spacetime oscillation, suggesting the *parametric resonance* of the field. Note that, for the frequency $\omega=50 \Lambda^{-1}$, there are two peaks at $f=50 \Lambda^{-1}$ (dominant peak) and at $f=100 \Lambda^{-1}$ (sub-dominant peak) frequencies. The second peak is arising may be due to the coefficient $\sin(2\omega t)$ of the first time derivative term in Eq.(6). For $\Phi_0=0.1 \Lambda^{-1}$ and $\lambda=4$, the amplitude of oscillation of ϕ_1 zero-mode is too small to determine such peak structure, therefore we haven't shown the frequency spectrum for it.

Fig.9 shows the frequency spectrum of zero-mode of field ϕ_2 in the same time interval as mentioned in Fig.8 for different spacetime oscillation frequencies ω (the time interval $t_i - t_f$ for each frequency ω has been mentioned in brackets). Unlike Fig.8, in this case, there is no background frequency spectrum. In figure, violet(dotted), green(solid thin), and black(solid thick) lines correspond to the frequency spectrum for 20, 50, and 100 Λ^{-1} frequencies of spacetime oscillation, respectively. In this case, each frequency spectrum peaks at half of the spacetime oscillation frequency ω . For $\omega=20 \Lambda^{-1}$, there is no unique and strong peak structure in the frequency spectrum. We have also checked that the real and imaginary part of higher momentum-modes of ϕ_2 (e.g. field-modes at $k_x=\omega/2, k_y=0$ and $k_x=0, k_y=\omega/2$; see Fig.7) also oscillates with the frequency $\omega/2$. In Fig.9, red(dashed) line corresponds to the case for which $\omega=100 \Lambda^{-1}$, $\Phi_0=0.1 \Lambda^{-1}$, and $\lambda=4.0$. In this case also, frequency spectrum peaks at the half of ω , shows the independence from the

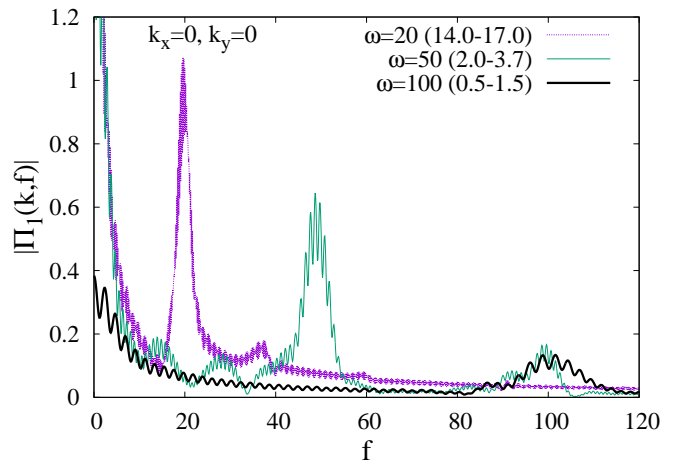


FIG. 8: Figure shows the frequency spectrum of ϕ_1 zero-mode for different spacetime oscillation frequencies ω in the time interval in which it oscillates with a significant large amplitude. This time interval for the respective frequencies has been written in brackets. Violet(dotted), green(solid thin), and black(solid thick) plots correspond to the frequency spectrum for 20, 50, and 100 Λ^{-1} frequencies of spacetime oscillation, respectively. It is very clear in each case, that frequency spectrum has a peak at the corresponding frequency ω of spacetime oscillation, which indicates the phenomena of *parametric resonance* of the field.

shape of the effective potential.

With all these results, it is clear that under the spacetime oscillation, the field Φ itself starts performing oscillation, in space and time, with certain momentum and frequency, by following the resonance condition for a given ω , where ϕ_1 field oscillates with frequency ω , while ϕ_2 with frequency $\omega/2$. This shows that the field Φ undergoes *parametric resonance* under the spacetime oscillation.

B. Frequency dependence of generation of field excitations

As we have discussed earlier, to generate longitudinal excitations, the frequency of spacetime oscillation should be $\omega \gtrsim m_\Phi$. In contrary to this, for transverse modes of the field, there is no such frequency cut-off as the mass of these modes is zero. In the equation of motion Eq.6, spacetime oscillation mainly couples with the gradient of the field. Therefore even in the low frequency regime, i.e. $\omega < m_\Phi$, spacetime oscillation can lead to the generation of transverse excitations via the parametric resonance. Thus, there is a fundamental difference in the evolution of field configuration in the frequency regimes $\omega \gtrsim m_\Phi$ and $\omega < m_\Phi$, and in both the regimes, in principle, field excitations can be generated under the spacetime oscillation.

In our simulation, we have studied the generation of field excitations and the formation of vortex-antivortex

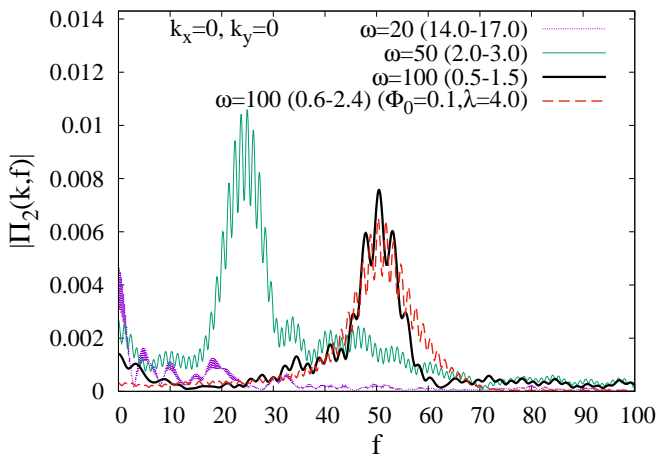


FIG. 9: Figure shows frequency spectrum of ϕ_2 zero-mode for different spacetime oscillation frequencies ω in the time interval as mentioned in Fig.8 (in brackets, mentioned here as well). Violet(dotted), green(solid thin), and black(solid thick) plots correspond to the frequency spectrum for 20, 50, and 100 Λ^{-1} frequencies of spacetime oscillation, respectively. The peak structures show that the zero-mode of ϕ_2 oscillates with $\omega/2$. Red(dashed) plot corresponds to the case, $\omega=100 \Lambda^{-1}$, $\Phi_0=0.1 \Lambda^{-1}$, and $\lambda=4$, which also peaks at $\omega/2$.

pairs in a wide range of frequencies of spacetime oscillation. At low frequencies, vortex-antivortex pairs form with relatively smaller vortex densities and remain well separated. In this regime, unlike the case of high frequency, field remains close to the VEV of effective potential for a significant time of evolution. This has been depicted in Fig.10, where left panel shows the vector plot of field configuration in the physical space and right panel shows the field distribution in the field-space; both are at time $t=18.5 \Lambda$. For this simulation, the spacetime oscillation frequency is taken $\omega=20 \Lambda^{-1}$, and other parameters of simulation are $\varepsilon=0.4$, $\Phi_0=10 \Lambda^{-1}$, $\lambda=40$ (same as used previously). Left plot clearly shows the formation of well separated vortex-antivortex pair in the system. Right plot shows that in almost all lattice points, the field is close to VEV of the effective potential, and the field distribution covers the whole vacuum manifold (starting from a localized distribution). It shows that mainly transverse excitations have been generated in the system, while longitudinal excitations are strongly suppressed in this frequency regime; compare with Fig.2(d).

We mention that in the low frequency regime, finite size of the system affects the generation of field excitations. This happens because the spacetime oscillation dominantly couples to k -modes of the field, where for ϕ_2 field ($k_{x(y)}=\omega/2$, $k_{y(x)}=0$)-modes grow with time; see Fig.4 and Fig.5. However for finite lattices with periodic boundary condition, the lowest non-zero k -mode which can be present in each direction is $k_L=2\pi/L$, where L is the lattice size. Therefore any frequency ω below the

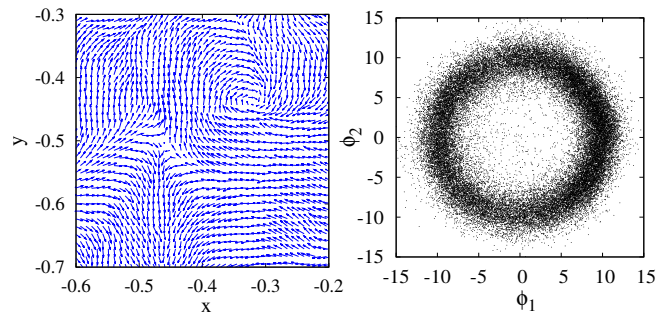


FIG. 10: Figure shows the field configuration in physical space (left panel) and in field-space (right panel) at time $t=18.5 \Lambda$ for the frequency $\omega=20 \Lambda^{-1}$ ($\varepsilon=0.4$, $\Phi_0=10 \Lambda^{-1}$, and $\lambda=40$). Left plot shows the formation of well separated vortex-antivortex pair in the system. Right plot shows that at this frequency of spacetime oscillation, mainly transverse excitations of the field has been generated.

cut-off $2k_L$ cannot generate resonant oscillation of the field; excitations with wavelength larger than lattice size can not be accommodated. Even with frequencies two or three times larger than this cut-off, the field finds difficulties to get excited. We have checked, that increasing lattice size leads to generation of excitations with a spacetime oscillation frequency, at which excitations can not be generated on smaller lattices. This suggests that in principle, any low frequency of spacetime oscillation can excite the field leading to the formation of vortices, if a suitable system size is chosen, and evolved for a significantly large time.

We have also studied the effect of using specific boundary condition on the generation of field excitations. For all results presented in this paper, we have used *periodic boundary condition*. We have seen that by using the fixed boundary condition (where the field at the boundary doesn't evolve), field gets excitations in relatively shorter time in comparison with using the periodic boundary condition. For example, with fix boundary condition, we have seen the formation of vortices in reasonably short time at $\omega=20 \Lambda^{-1}$ on 150×150 lattice, which we have never seen by using *periodic boundary condition* on the same lattice and with the same ω . Note that the *fix boundary condition*, with a suitable profile of the condensate field, is an appropriate boundary condition for the evolution of superfluid phase inside a neutron star. So this boundary condition may help the generation of excitations and formation of superfluid vortices inside neutron stars during the BNS merger.

C. The time dependence of formation of vortices on frequency and amplitude of spacetime oscillation

In this section, we present our study on the dependence of the parameters of spacetime oscillation in the formation of vortices. For this, we note down the time t_{vortex}

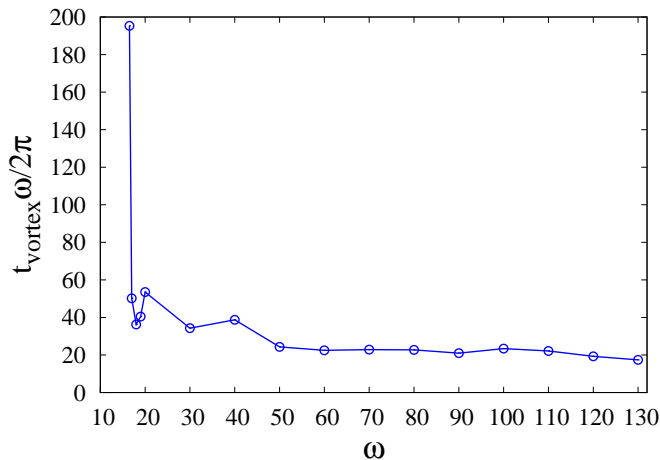


FIG. 11: Figure shows the dependence of vortex formation time t_{vortex} on various frequencies ω . In figure, we have plotted the *number of cycle* of spacetime oscillation up to the time t_{vortex} , i.e. $t_{vortex} \omega / 2\pi$, versus ω . For this plot, parameters are, $\varepsilon=0.4$, $\Phi_0=10 \text{ \AA}^{-1}$, and $\lambda=40$. Figure clearly shows that in the frequency regime $\omega \gtrsim 50 \text{ \AA}^{-1}$, $t_{vortex} \omega / 2\pi$ is almost independent from ω . However, by decreasing the frequency ω below 50 \AA^{-1} , this number starts increasing.

at which the first vortex-antivortex pair forms in the system. We call this time as the *vortex formation time*. To locate the vortices, we compute the variation of phase of Φ around each elementary square of lattice. The variation of phase between any two adjacent points on the elementary square is determined by the *geodesic rule* [23]. By continuity, the phase of a complex scalar field along a loop is always $2\pi n$, where n is an integer. Throughout the evolution of field, we observe only $n=0, \pm 1$ for the variation of phase around each elementary square. We identify the vortex with $n=+1$ and antivortex with $n=-1$. We have checked that t_{vortex} doesn't much depend on the amplitude of fluctuations in the initial field configuration, i.e. on β .

In Fig.11, we have plotted $t_{vortex} \omega / 2\pi$ versus ω for $\varepsilon=0.4$. The parameters of the effective potential are $\Phi_0=10 \text{ \AA}^{-1}$ and $\lambda=40$. Note that $t_{vortex} \omega / 2\pi$ is a dimensionless number which is equal to the *number of cycle* of spacetime oscillation up to the time t_{vortex} . Figure clearly shows that in the frequency regime $\omega \gtrsim 50 \text{ \AA}^{-1}$, the *number of cycle* required to form vortices is almost independent from ω . However, by lowering the frequency of spacetime oscillation below 50 \AA^{-1} , this number starts increasing. We haven't seen the formation of any vortices below $\omega=16 \text{ \AA}^{-1}$ up to a significantly large time on the used lattice.

We have already mentioned, that in the low frequency regime, finite size of the system plays an important role in the generation of field excitations and therefore formation of vortices as well. For example, in our simulation, up to a significantly large time, there is no formation of any vortex-antivortex pair on 200×200 lattice at fre-

quency $\omega=15 \text{ \AA}^{-1}$, however with the same parameters of simulation, vortices form on 800×800 lattice. Therefore, it may be possible that the deviation of $t_{vortex} \omega / 2\pi$ from a constant value below $\omega=50 \text{ \AA}^{-1}$ in Fig.11 arises due to the finite size effects of the system. Therefore, it may also be possible that this constant value is a universal number for the formation of vortices and may remain true even in the low frequency regime when the finite size effects get eliminated. However, more detailed investigations are needed, which we will try to pursue in the future work.

To investigate the dependence of t_{vortex} on system size, we note down t_{vortex} for various system sizes by keeping $\omega=20 \text{ \AA}^{-1}$ (here we haven't shown the plot for this). We find that t_{vortex} is overall monotonically decreasing function of system size. However, there are system sizes where this monotonicity gets violated. This shows that there are much more complexity involved in the generation of field excitations and formation of vortices. We will try to explore this investigation in more detail in our future work. Despite of all this, our present investigation suggests that even with a small frequency ω , field may get excited (transverse excitations) if one performs simulation on a significantly large lattice and for a significantly large time.

In Fig.12, we have presented the effect of ε on t_{vortex} . For this plot, we have taken $\omega=100 \text{ \AA}^{-1}$, $\Phi_0=10 \text{ \AA}^{-1}$, and $\lambda=40$. Figure clearly shows that decreasing ε causes more time to form vortex-antivortex pair in the system. By decreasing ε , system takes longer time to achieve field excitations, and the large amplitude field oscillation stage persists for a longer time. In the regime of very small ε , the field excitations don't grow sufficiently to create vortices in the system. This behavior of field response to ε is also a feature of *parametric resonance*, in which the resonant growth is strongly suppressed by decreasing the magnitude of time dependent parameter(s) of the oscillator [22].

D. Formation of vortex-antivortex lattice under spacetime oscillation

The formation of vortex-antivortex lattice structure has interest in various condensed matter systems. In refs.[24–26], the formation of such lattices has been studied in superconducting films with magnetic pinning arrays, ultra-cold fermionic gases in two-dimensions, and superconducting twisted-bilayer graphene. The melting of vortex-antivortex lattice in two-dimensional Fermi gases has been studied in ref.[27]. For certain parameters of the simulation, we have also seen the formation of vortex-antivortex lattice structure under the spacetime oscillation. In Fig.13, we have shown the phase (left panel) and magnitude (right panel) of the field Φ at two different times of field evolution. The parameters of the

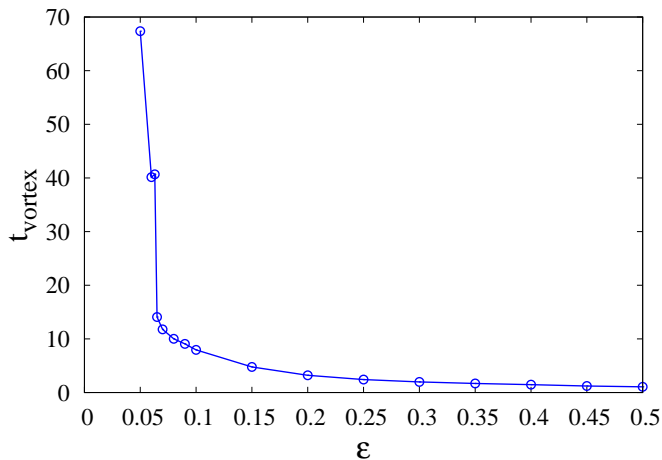


FIG. 12: Figure shows the effect of ϵ on t_{vortex} . For this plot, we have taken $\omega=100 \text{ \AA}^{-1}$, $\Phi_0=10 \text{ \AA}^{-1}$, and $\lambda=40$.

simulation are $\omega=17 \text{ \AA}^{-1}$, $\epsilon=0.4$, $\Phi_0=0.1 \text{ \AA}^{-1}$, and $\lambda=4$. Fig.13(1a) and Fig.13(1b) show the phase and magnitude of the field Φ at time $t=28.65 \text{ \AA}$, while Fig.13(2a) and Fig.13(2b) show the same at time $t=29.4 \text{ \AA}$. On the plots, circles and triangles indicate the location of vortices and antivortices, respectively. Correspondingly, in the left panel, there is a variation of $\pm 2\pi$ in the phase of Φ at the location of these points. The $\pm 2\pi$ phase variations correspond to the vortex and antivortex configurations, respectively. In the right panel, these points correspond to the places where the magnitude of Φ is zero. One can clearly notice that there is a vortex-antivortex lattice structure in both, upper and lower, panels. We have seen, that this lattice structure keeps on changing with time. We have checked that the formation of this structure has nothing to do with the amplitude of initial fluctuations, i.e. on the value of β . It may be possible that such lattice structure is arising because of using the periodic boundary condition in the simulation.

V. CONCLUSION AND FUTURE OUTLOOK

In this work, we have performed (2+1)-dimensional simulations for a complex scalar field in the presence of oscillating spacetime metric background. We have considered spacetime metric as a time-dependent periodic perturbation on the top of the Minkowski metric. The field is taken on the VEV of U(1) symmetry breaking effective potential, and small spatial fluctuations in the initial field configuration has been considered. We see that depending upon the amplitude and frequency of the metric, field undergoes *parametric resonance* causing the generation of field excitations, which ultimately lead to the formation of vortex-antivortex pairs in the system. We find that there is a fundamental difference in the evolution of field in the frequency regimes $\omega \gtrsim m_\Phi$ and

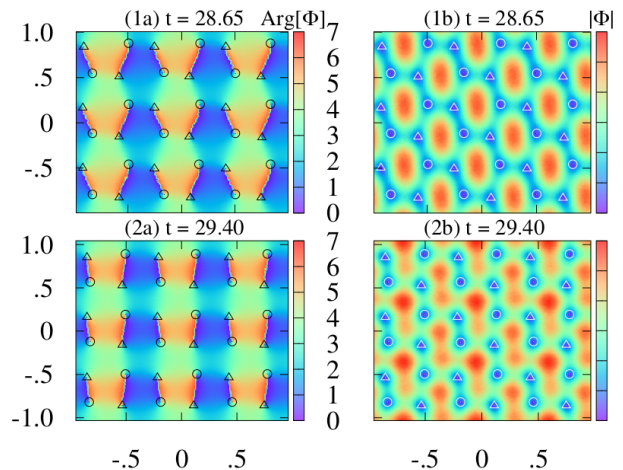


FIG. 13: Figure shows the formation of vortex-antivortex lattice structure in the system. The parameters of the simulation are $\omega=17 \text{ \AA}^{-1}$, $\epsilon=0.4$, $\Phi_0=0.1 \text{ \AA}^{-1}$, and $\lambda=4$. Plots (1a) and (1b) show the phase and magnitude of field Φ at time 28.65 \AA , while plots (2a) and (2b) show the same at time 29.4 \AA . With the distribution of phase and magnitude of field, one can notice a structure of vortex-antivortex lattice, which has been depicted by pointing the locations of vortex and antivortex with circles and triangles, respectively.

$\omega < m_\Phi$. In the low frequency regime mainly transverse excitations arise, and well separated vortex-antivortex pairs form in the system. While in the high frequency regime, longitudinal excitations of the field also get generated.

In our simulation, finite size of the system restricts the generation of field excitations in the low frequency regime of spacetime oscillation. However, our study suggests that in principle any low frequency can excite the field if suitable system size is chosen, and field is evolved for a significantly large time. We have studied the frequency dependence of the *number of cycle* of spacetime oscillation required to form a vortex-antivortex pair in the system. We find that in relatively high frequency regime, this number is independent from the frequency of spacetime oscillation and remains constant (seems to be a universal number). However, in the low frequency regime, due to the finite size effect, this number gets a strong deviation from this constant value, and increases by decreasing frequency. The formation of vortices also depends on the amplitude of spacetime oscillation; the vortex formation time increases by decreasing amplitude. For certain parameters of the simulation, we have also seen the formation of vortex-antivortex lattice structure.

Throughout this work, we have completely ignored the back reaction of energy density perturbations of the field, arise due to spacetime oscillation, on the spacetime metric. As we see the formation of vortices in our simulation, and a vortex configuration carries an energy density profile with maximum value in the vortex core. Therefore depending upon the energy of the configuration, it can

cause changes in the spacetime manifold, which can affect the further evolution of the field. It will be interesting to see how the field evolves under this complete scenario. We will try to pursue this in our future work.

To study the time evolution of the condensate field for neutron stars superfluidity during the BNS merger, a full (3+1)-dimensional simulation with an appropriate time dependent deformation of star metric is required. It will disclose whether the time scale and length scale of the whole process are sufficient to excite the condensate field to lead the formation of vortex-antivortex pairs in the interior superfluid. We plan to pursue the phenomenological application of our present study for this system in the future work.

The present work has its applications in other systems also. For example, since the *second homotopy group* of S^2 -manifold is non-trivial, i.e. $\pi_2(S^2)=\mathbb{Z}$ [3], therefore this manifold allows the existence of *topological texture* in (2+1)-dimensions (baby Skyrminion) and *topological monopole* in (3+1)-dimensions. Similarly, S^3 -manifold (group space of $SU(2)$) allows the existence of *topological texture* in (3+1)-dimensions as the *third homotopy group* $\pi_3(S^3)=\mathbb{Z}$ [3]. These topological objects have their cosmological interests, formation of which, can also be studied under the spacetime oscillation (similar to the formation of vortices presented in this paper). In the *abelian-Higgs model* and pure $U(1)$ gauge theory also, one can study the formation of flux-tubes and generation of magnetic field, respectively, under this oscillation.

This study can also be extended for the $U(1)$ -symmetry broken effective potential with a small explicit symmetry breaking term. In this case, for the generation of field excitations, there must be a lowest frequency cut-off of spacetime oscillation set by the mass of pseudo-Goldstone modes; only frequencies higher than or equal to the mass of these modes can lead the field excitations. In our simulation, we have seen the field excitations in the presence of such term (we haven't presented this here). This result can be utilized in the generation of excitations of the *axion-like* field carrying mass $\sim 10^{-22} - 10^{-21}$ eV [28] and coupled with the spacetime oscillation. The *axion-like* particles having above mass range are considered to be a possible dark matter candidate, known as the 'wave dark matter' or 'fuzzy dark matter' (FDM) [28]. To excite this field, correspondingly, the frequency of spacetime oscillation should be $\gtrsim 10^{-4} - 10^{-3}$ Hz. This can be easily achieved by the BNS [15] and black-hole merger [29] systems, which produce gravitational wave (GW) in the frequency range of ~ 10 Hz - 1 kHz with a significantly large strain amplitude. We expect that a sustained spacetime oscillation will give rise excitations of *axion-like* field over a length scale having momentum of field corresponding to the frequency of spacetime oscillation. The effect will be more pronounced in the closest region of GW source as the strain amplitude is significantly large there. If such excitations arise, then the field will start oscillating co-

herently and decay to the vacuum of effective potential. This leads to the coherent emission of *axion-like* particles from various constant- r hypersurfaces about the source. We will present this phenomena in detail in our future work.

ACKNOWLEDGEMENTS

We are very grateful to Ajit M. Srivastava and Subhronel Chakrabarti for very useful discussions, suggestions, and comments on the manuscript. We also would like to thank A.P. Balachandran, P.S. Saumia, Abhishek Atreya, T.P. Sreeraj, Nirupam Dutta, and Minati Biswal for useful discussions and comments on the work.

* Electronic address: shreyanshsd@imsc.res.in

† Electronic address: digal@imsc.res.in

- [1] W.H. Zurek, Phys. Rep. **276**, 177 (1996).
- [2] A. Rajantie, Int. J. Mod. Phys. **A17**, 1 (2002).
- [3] N.D. Mermin, Rev. Mod. Phys. **51**, 591 (1979).
- [4] T.W.B. Kibble, J. Phys. **A9**, 1387 (1976); Phys. Rept. **67**, 183 (1980).
- [5] L.D. Landau and E.F. Lifshitz, **Statistical Physics Part 2**, Pergamon Press Ltd. (1980).
- [6] D.R. Tilley and J. Tilley, **Superfluidity and Superconductivity**, Third Edition, Overseas Press (2005).
- [7] S. Digal, R. Ray, S. Sengupta, and A.M. Srivastava, Phys. Rev. Lett. **84**, 826 (2000).
- [8] R. Ray and S. Sengupta, Phys. Rev. D **65**, 063521 (2002).
- [9] E.A.L. Henn, J.A. Seman, G. Roati, K.M.F. Magalhães, and V.S. Bagnato, Phys. Rev. Lett. **103**, 045301 (2009); E.A.L. Henn et al., Phys. Rev. A **79**, 043618 (2009).
- [10] V.I. Yukalov, A.N. Novikov, V.S. Bagnato, Phys. Lett. A **379**, 1366 (2015).
- [11] V.I. Yukalov, E.P. Yukalova, and V.S. Bagnato, Phys. Rev. A **66**, 043602 (2002).
- [12] R.E. Packard, Phys. Rev. Lett. **28**, 1080 (1972).
- [13] D.G. Yakovlev, A.D. Kaminker, and K.P. Levenfish, Astron. Astrophys. **343**, 650 (1999).
- [14] M.G. Alford, A. Schmitt, K. Rajagopal, and T. Schäfer, Rev. Mod. Phys. **80**, 1455 (2008).
- [15] B.P. Abbott et al. (LIGO Scientific Collaboration and Virgo Collaboration), Phys. Rev. Lett. **119**, 161101 (2017).
- [16] **Gribov-80 Memorial Volume; Quantum Chromodynamics And Beyond**, C.N. Colacino, page 449-454, World Scientific (2010).
- [17] A. Perego, S. Bernuzzi, and D. Radice, Eur. Phys. J. A **55**:124 (2019).
- [18] J. Anandan, Phys. Rev. Lett. **47**, 463 (1981).
- [19] A. Schmitt, **Introduction to Superfluidity; Field-theoretical Approach and Applications**, Springer (2015).
- [20] C. Xiong, M.R.R. Good, Y. Guo, X. Liu, and K. Huang, Phys. Rev. D **90**, 125019 (2014).
- [21] S. Carroll, **Spacetime and Geometry; An Introduction to General Relativity**, Addison Wesley (2004).

- [22] L.D. Landau and E.F. Lifshitz, **Mechanics; Third Edition**, Elsevier (2007).
- [23] M.J. Bowick, L. Chandar, E.A. Schiff, and A.M. Srivastava, *Science* **263**, 943 (1994); [hep-ph/9208233].
- [24] M.V. Milošević and F.M. Peeters, *J. Low Temp. Phys.* **139**, 257 (2005).
- [25] S.S. Botelho and C.A.R. Sá de Melo, *Phys. Rev. Lett.* **96**, 040404 (2006).
- [26] Y. Su and S.-Z. Lin, *Phys. Rev. B* **98**, 195101 (2018).
- [27] G. Cao, L. He, and X.-G. Huang, *Phys. Rev. A* **96**, 063618 (2017).
- [28] L. Hui, J.P. Ostriker, S. Tremaine, and E. Witten, *Phys. Rev. D* **95**, 043541 (2017).
- [29] B.P. Abbott et al. (LIGO Scientific Collaboration and Virgo Collaboration), *Phys. Rev. Lett.* **116**, 061102 (2016).